Linear investigation of sound-flow interaction along a corrugated plate

Massimo D'elia, Thomas Humbert, Yves Aurégan

Linear investigation of sound-flow interaction along a corrugated plate

Massimo E. D'Elia [1,*], Thomas Humbert, Yves Aurégan

Laboratoire d'Acoustique de l'Université du Mans (LAUM), Avenue Olivier Messiaen, 72085 Le Mans Cedex 9, France

Abstract

The experimental investigation of the aeroacoustic behaviour of a corrugated plate with small cavities in presence of a grazing flow is discussed. In particular, the linear regime of the aeroacoustic interaction has been investigated. The obtained Strouhal number corresponds to those used in the recent literature for nonlinear investigations. Even if acoustic feedback was eliminated in the experimental setup, loss and gain frequency bands can still be identified. Then, the acoustic and Laser Doppler Velocimetry (LDV) measurements were used to analyse the acoustic power at four different frequencies: the four components that compose the acoustic power have been characterised and their relative importance identified. Finally, the difference behind gain and loss mechanisms are spotted and explained.

Keywords: Aeroacoustics, Corrugated pipes, Duct acoustics, Hydrodynamic modes

1. Introduction

Corrugations are a technological solution used to meet the needs for strength and flexibility of pipes in industrial applications (e.g. gas extraction). However, intense whistling can occur in these pipes, which can lead to fatigue-related failures and noise disturbances [1, 2]. The first investi-

*Corresponding author
Email address: Massimo_Emiliano.dElia.Etu@univ-lemans.fr (Massimo E. D'Elia)
[1] *Permanent Address*: massimo.e.delia@gmail.com

gations on corrugated tubes focused on the whistling behaviour in order to identify the main parameters underneath. The driving mechanism inducing whistling is a feedback-loop between two systems, a fluid-dynamic and an acoustic one. The free shear layer past a cavity is unstable and could self sustain when encountering the trailing edge of the cavity, thus behaving as a sound amplifier. When the natural frequency of this amplifier is close to one of the acoustic resonant frequencies of the corrugated tube, then an energy transfer is possible and a feedback loop is created (see for example [3, 4, 5] and Figure 1 for a schematic image where f_v is a general feedback frequency). Specifically, the acoustic system act as a filter, as the standing wave resonant frequencies are discrete, amplification can be obtained around these discrete points. It is possible to identify a linear and a nonlinear amplification regime. The latter is characterised by large and finite vortex structures that can produce whistling and the acoustic power grows linearly with the amplitude of the hydrodynamic perturbations. In the linear regime, on the other hand, vorticity is at a smaller scale, while the acoustic power grows quadratically with hydrodynamic perturbations amplitudes. Recent literature has focused mainly on whistling and the nonlinear regime, in order to characterise this striking effect, both from an experimental and numerical point of view. In [6], the amplification characteristic Strouhal numbers were identified, as well as the saturation mechanism of the perturbation velocity which separates linear and nonlinear behaviours. Several other works [7, 8, 9, 10, 11] investigated the details of corrugated walls and side cavity branches in their similarities and differences. In all these works, a detailed analysis of the literature focused on the nonlinear regime can be found. In the case of moderate to high amplitude perturbations the shear layer vorticity concentrates into discrete vortices shed at the upstream edge of the cavity. To model this behaviour a Discrete Vortex (DV) model has been developed[12, 13, 14]. One of the first application is shown in [15], where a single vortex is shed everytime the acoustic velocity changes its direction inward/outward the cavity. This vortex then moves at constant velocity along the cavity width. In this model, the vortex convective speed is an empirical parameter of the problem and therefore also the Strouhal number. In a different approach [16], vorticity can be thought as distributed along an infinitely small shear layer in a Continuous Vortex (CV) model: the distributed vorticity eliminates the vortex singularity at the upstream edge of the cavity. In [17], this model improves the estimations of the acoustic power when compared with the results from [14]. However, also in this case, the lenght of the vorticity strip is inherently

an empirical parameter to be fitted.

Regarding the linear regime, on the other hands, literature lacks both experimental and theoretical results. Experimental data of the linear aeroacoustic field in the linear regime are scarce (e.g. [18]) and they give mainly a global analysis of the aeroacoustic interaction. Theoretical works based on the stability theory from [19] tried to assess the shear layer perturbation due to the acoustic forcing but failed in explaining fundamental effects. Others, like in [20], used an infinitely small shear layer whose vertical displacement represents the driving mechanism for the cavity oscillations due to the Kelvin-Helmholtz instability. In all cases, the difference w.r.t. experimental data remains large.

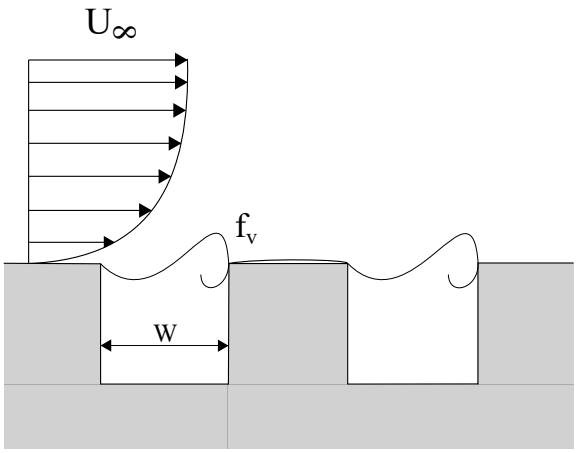

Figure 1: Schematic view of the impinging mechanism along a corrugated surface.

Therefore, the main target of the present study is to retrieve, by means of Laser Doppler Velocimetry (LDV), the aeroacoustic field inside a single cavity of a corrugated plate operating in a linear regime and check whether the aforementioned models remain applicable. For this reason, a configuration with small cavities and small amplitude perturbations have been chosen in a non-whistling case. In sections 2.1 and 2.2, the experimental rig and the investigated corrugated plates are introduced. In section 3, the velocity retrieval process through the LDV technique is presented. Finally, acoustic and optical results, as well as the retrieved acoustic power, are presented in section 4.

All LDV and acoustic measurements can be found at [21].

2. Experimental Setup

2.1. Test Rig

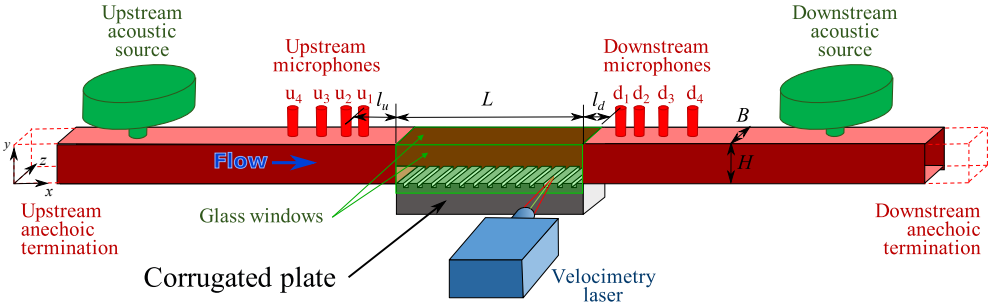

Figure 2: Schematic view of the experimental setup.

The test rig is a uniform rectangular duct whose section is $B = 50$ mm $\times$ $H = 40$ mm, see Fig. 2. In this duct, a mean flow is produced by a centrifugal fan whose flow rate can be continuously adjusted up to a mean velocity of 85 m s^{-1}. The flow velocity is measured by a Pitot tube (diameter 2.1 mm) in the center of the rectangular duct and by Laser Doppler Velocimetry (LDV). The duct has upstream and downstream anechoic terminations which ensure low reflection coefficients on both side of the studied corrugated plate. The upstream anechoic termination is sealed to prevent any leakage of the mean flow. From this upstream termination up to the studied element, a 1.90 m long smooth rigid pipe segment is installed to allow a complete development of the flow. The investigated element is located in a test section of length $L = 200$ mm. To allow access for optical measurements, a side wall and the top wall are made of glass, the floor being the position of the tested acoustic treatments that can be easily changed. Downstream of the test section, a second rigid duct segment connects to the downstream anechoic termination. The sound field is produced by a compression driver (Beyma CP850Nd) which can provide an acoustic level up to 150 dB SPL in the test section over a frequency range going from 500 to 4000 Hz. The acoustic source can be placed either upstream or downstream of the studied element in order to obtain two different states of the system.

The test rig has been conceived so that both acoustic and optical measurements can be carried out exactly on the same test section and sample. In order to determine the tested element transmission and reflection coefficients, $T^{\pm}$ and $R^{\pm}$, the upstream and downstream rigid ducts are equipped

with 4 microphones each. This allows an over-determination of the incoming and outgoing acoustic waves upstream and downstream of the tested element [22]. Using the two acoustic sources to obtain two different acoustic states of the system [23], the four elements of the scattering matrix for plane waves (transmission and reflection coefficients on both directions: $T^{\pm}$ and $R^{\pm}$) can be evaluated.

A 2D Laser Doppler Velocimetry (LDV) Dantec Dynamics 2D FlowExplorer system is used to measure the vertical (v along y) and horizontal (u along x) velocities inside a selected cavity (see Figure 2). Its lasers wavelengths are of 532 and 560 nm at a f = 300 mm focus length. The system has a measurement volume of 0.7 mm^3 and its support system is capable of displacing with a spatial resolution of 0.10 mm. Therefore, the attainable spatial resolution inside the cavity is hardly beatable by other (optical and not) techniques. One main constraint in applying such a technique to small corrugations is the finite angle between the laser beams. Indeed, as we are interested in measuring as close as possible to the horizontal and vertical wall, it is important to tilt the LDV system. This is achieved, vertically, by rotating the LDV sytem of a compensating angle β which must be greater than half the angle between the laser beams (this is schematically shown in Figure 3). On the other hand, for measuring as close as possible to the vertical walls, and yet be as close as possible to the duct centerline, it is necessary to carry out the measurements in two sub-domains, each accounting for half of the cavity (again, schematically displayed in Figure 3 using the angle α). In this way, the interference between the laser beams and the rigid walls is avoided (at least inside the measurement area of interest). These tilt angles are very small as they are equal to the half-angle between the laser beams and they are compensated for during the post-processing of the data. Once these constraints are taken into account, measurements can be carried out: the LDV system comes together with a Burst Spectrum Analyzer (BSA) Dantec Dynamics software which manages the laser position in space and the acquisition procedure. Regarding the latter, main attention has to be given to the synchronization between the laser and the acoustic source, in order to have measurements throughout the whole reference signal period. This can be done by a phase-locked approach but, in order to reduce errors (e.g. data folding over one period), and as we are working at one frequency at the time, a simpler approach was used. For the latter, a source signal produced by a frequency generator feeds both the loudspeaker through an amplifier and the LDV trigger entrance. This feeding signal is also reacquired into the LDV

acquisition system (in order to always know the reference electronic signal that is given to the system). In this way, we can produce a single frequency signal in the duct while having a reference trigger for the acquisition system always identically syncronised at the same time reference. This appears to be even more important when we have to correlate two sub-volumes data, as mentioned before.
Finally, scattering particles are needed to measure quantities inside the duct. Here, incense has been used since it produces smoke particles with favorable diameters [24], [25],[26]. Indeed, the corresponding Stokes number is about $St \sim 0.006 - 0.008$, if we also consider the typical forcing frequency of 2 kHz and a dynamic viscosity of air of $\nu = 1.81 * 10^{-5}$ kg m^{-1} s^{-1}. This value is obtained by applying the formula:

$$St = \left(\frac{\omega}{\nu}\right)^{\frac{1}{2}} d_p, \tag{1}$$

from [27], where ω is the forcing frequency and d_p the particle diameter.

2.2. Corrugated Walls

The studied corrugated plate is shown in Figure 3-b. It is a 200 mm long anodized plate characterized by an array of 16 cavities: each cavity measures 4x4x50 mm^3 (covering the entire transverse span B = 50 mm of the duct), has square and sharp edges on both sides and is separated by a 12 mm pitch. The cavity investigated is the third from the end of the plate (w.r.t. the flow direction) because here the boundary layer is fully developed.

To have a phase reference, the horizontal periodic velocity u'_{ref} was measured away from the corrugations in the central part of the duct (reference box on Figure 4-a). Indeed, in the central part of the duct, it is possible to consider that the hydrodynamic disturbances are low and that the horizontal periodic velocity is only due to the acoustics. Thus, the value of the horizontal acoustic velocity (averaged over the reference box) was taken as a reference for the amplitude of the incident acoustic wave and, more importantly, as a phase reference that does not depend on the acoustic path between the source and the measurement position. Therefore, all phase values presented in the following are taken relative to this reference.

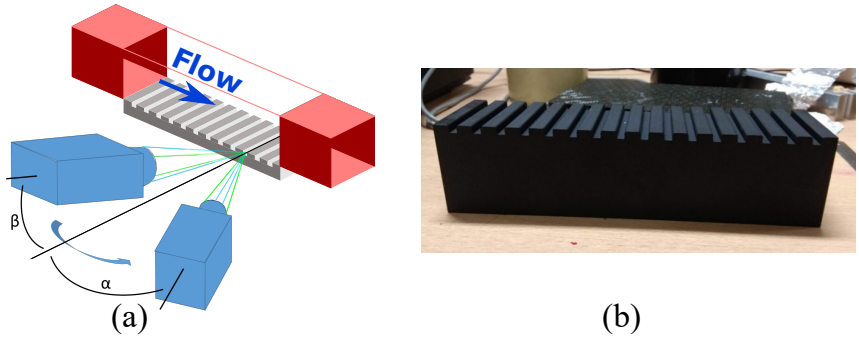

Figure 3: (a) Schematic view (not at scale) of the optical experimental setup and (b) picture of the investigated corrugated plate.

2.3. Mean Flow in the Setup

In this section, we look at the mean quantities associated to the flow. Figure 5-a,b and Figure 5-d,e display the mean horizontal and vertical velocity contours when the upstream source position is working at 1400 Hz and 2000 Hz. We can see that the velocity field is well resolved and there is no major difference between the two measurements in the mean velocity distribution. This is further confirmed in Figure 5-c, where the horizontal velocity is shown along the vertical lines indicated in open and filled symbols, which correspond to the lines for $x = 0, W/3, 2W/3, W$. We can see that the curves are similar for the two frequencies and that, outside the cavity, the velocity profile of the shear layer doesn't change with the longitudinal position. Equally important is to notice from the streamlines in Figures 5-d,e that this shear layer is layed out above a recirculation zone, regardless of the frequency case. In Figure 6-c, the velocity profiles along the vertical lines at $x = 0, W/3, 2W/3$ for the 2000 Hz case, are again shown, from inside the cavity up to the centerline of the channel. In this case, the velocity profiles are shown in the so called wall coordinates $y^+ = y\nu/U_\tau$ and $u^+ = U_0/U_\tau$, where ν is the dynamic viscosity of the air and U_τ is the friction velocity defined through the shear stress $\tau = \mu\, dU_0/dy|_w$ at the wall as $U_\tau = \sqrt{\tau}/\rho$. This velocity was obtained from the slope of the velocity inside the logaritmic layer [28, 29] and its value is found to be 1.01 m s^{-1}. Two layers are then identified: the above mentioned logaritmic layer, closer to the wall, and an external core layer, where the viscosity due to the turbulence ν_t is supposed to be constant.

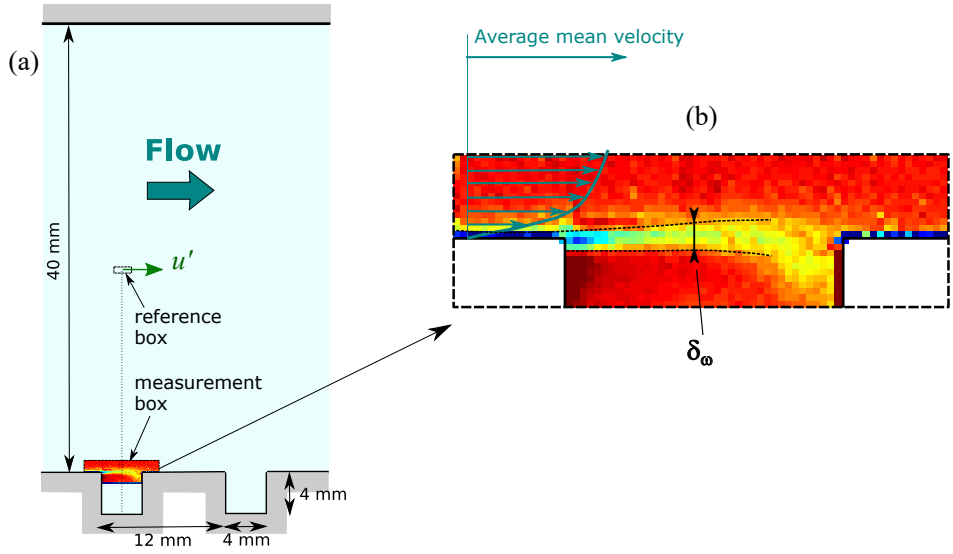

Figure 4: (a) Position of the measurement box and of the reference box. (b) Values of the mean vorticity for $M_\infty = 0.07$.

In the first, a velocity profile of the kind

$$u^+ = \frac{1}{K}\ln\left(\frac{1}{K} + y^+\right) + 5.5 \tag{2}$$

is obtained, while for the core layer, a parabolic profile is retrieved

$$\frac{U_\infty - U_0}{U_\tau} = \frac{HU_\tau}{2\nu_t}\left(1 - \frac{y}{H}\right)^2 \tag{3}$$

where H is the channel half-height and K is the von Karman constant, $K = 0.41$. These two layers match around $y^+ = 120$ (i.e. $y \approx 2$ mm) to which a $\nu_t = 8.02 \cdot 10^{-4}$ m^{2}s^{-1} corresponds. In Figure 6-b, a cavity close-up of the horizontal mean velocity U_0 along the same three lines is shown. The boundary layer outside the cavity seems to remain unchanged along the cavity length (for $y > 0.2$ mm), while this is not true for the shear layer inside the cavity itsef. Inside the cavity, the velocity changes until it reaches an almost steady value. Then, we can define the thickness of the shear layer as the distance between these two points. For the $x = 0$ position, this is roughly 0.6 mm, while for the $x = 2W/3$ mm this grows up to ≈ 1 mm.

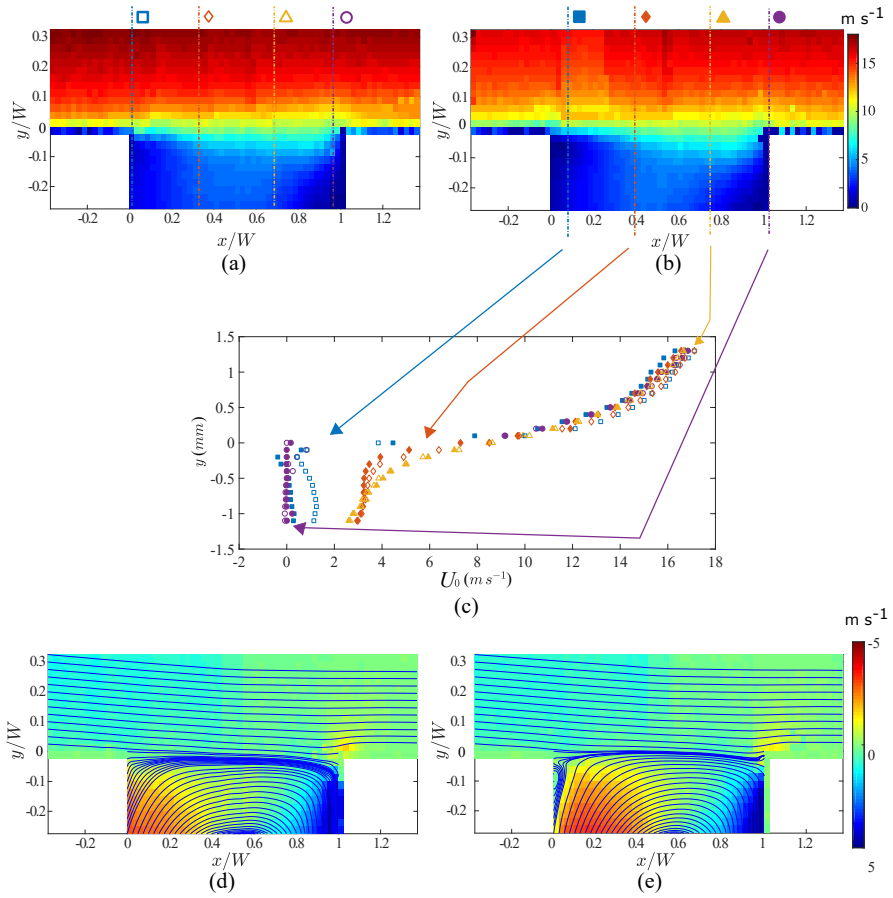

Figure 5: Horizontal mean velocity for the upstream source case at (a) 1400 Hz and (b) 2000 Hz. In (c) the velocity close to the cavity is shown along the vertical lines as indicated in the (a-b) Figures. The open and filled symbols represent the 1400 and 2000 Hz case, respectively. The vertical mean velocity has been shown for the (d) 1400 and (e) 2000 Hz cases, together with streamlines.

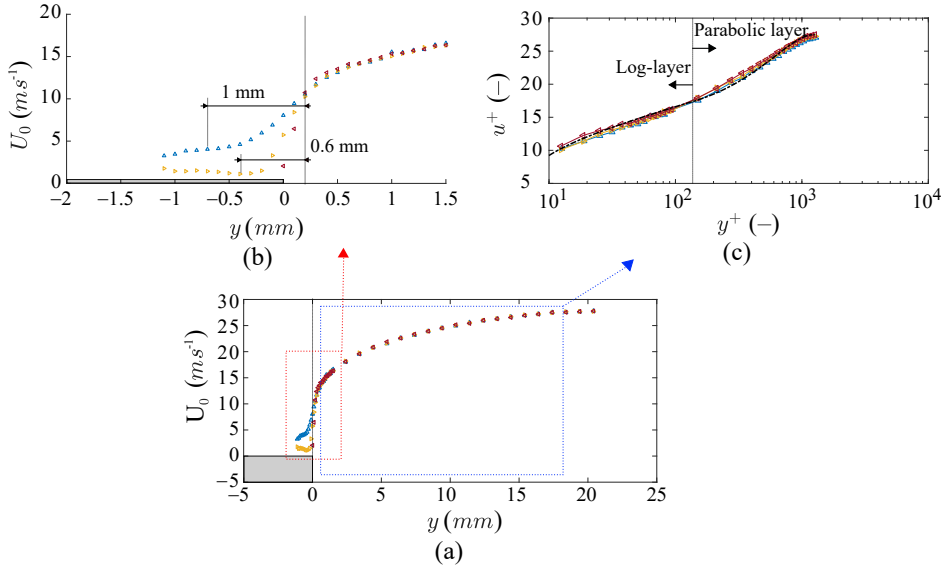

Figure 6: Horizontal mean velocity for the 2000 Hz upstream source case (a). The velocity is shown along three vertical lines corresponding to the $x = 0, 1/3W, 2/3W$ horizontal positions, to which the $\triangleleft$, $\triangleright$, $\triangle$ symbols corresponds. In (b) a zoomed figure of the same velocities inside the cavity is shown, while in (c) the analytical curves are plotted together with the experimental ones in wall coordinates.

2.4. Acoustic Velocity Modeling

As shown later in section 5, in the present configuration, the acoustic power can be described by the Howe analogy, which basically accounts for the interaction between a Coriolis force (i.e. the $-\rho_0 (\boldsymbol{\omega} \times \mathbf{u})$ term, where $\mathbf{u}$ and $\boldsymbol{\omega}$ are the total velocity and vorticity vectors, respectively, and ρ_0 the density of the fluid) and the acoustic velocity $\mathbf{u}_a$. As from the measurements it is not feasible to extract only the acoustic potential velocity component, it is necessary to obtain it through modelling. There are several ways of solving the compressible flow field, but a rather simple way was to use the commercial code COMSOL. To retrieve the acoustic velocity in quiescent conditions (as the Mach number considered is very small), the ACPR Module was used to solve the Helmholtz equation in frequency domain.

In Figure 7 we can observe the potential flowfield obtained for a single cavity: the net flow entering in the cavity is zero and the minimum and maximum velocity values appear at the leading and trailing edge, respectively. Since this is a potential flow, the velocity $\mathbf{u_s}$ in all points of the domain is defined w.r.t. a reference value. Therefore, we need to scale the simulated velocity to the actual velocity field at a reference "free stream" position (i.e. the "reference box" indicated in Figure 7). At this position, the measured horizontal coherent velocity component is the actual acoustic velocity.

3. LDV Experimental Investigation

3.1. Retrieving the Fluctuating Velocity Component

With the LDV technique it is possible to measure the velocity of a single scattering particle which crosses the measurement volume. During a given time interval, several particles goes through this volume and a velocity distribution is obtained. Moreover, the larger the data set, the more converged will the measurement distribution be. Therefore, for each measurement point, thousands of particle velocities have to be acquired in order to have a complete statistical representation of the velocity. This velocity has three main contributions

$$\mathbf{u} = \mathbf{U_0} + \mathbf{u'} + \mathbf{u_t} \tag{4}$$

which are respectively the time-averaged, the phase-averaged coherent and the turbulent velocity vectors. The phase-averaged component is the time

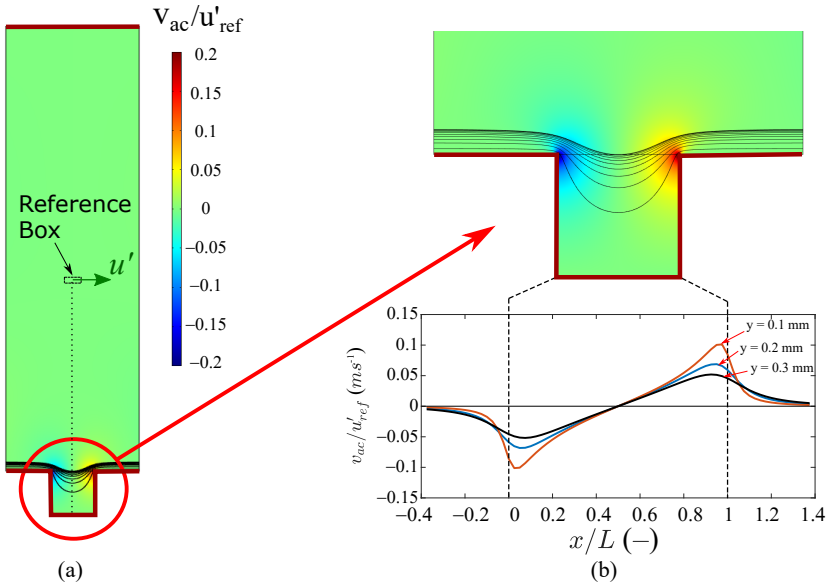

Figure 7: (a) Potential velocity field contour as obtained from the COMSOL simulation. The reference box indicates where the reference velocity was calculated. The (b) zoomed-in contour shows the velocity field close to the cavity while the underlying plot shows the potential velocity along three horizontal lines above the cavity lid.

dependent velocity at the frequency of the acoustic source and therefore will be described as

$$\mathbf{u}' = a' \sin\left(2\pi f_s t + \phi\right), \tag{5}$$

where f_s is the acoustic source frequency. The turbulent component $\mathbf{u_t}$ accounts for the remaining time dependent component inside the velocity signal.

In order to retrieve the periodic component of the velocity, measurements could be carried out through a phase locked approach, where different measurements at different positions along the signal feed cycle are needed. This implies that these data need to be folded inside the same cycle, introducing a truncation error. In our case, as the signal frequency is known and constant, we decided to directly investigate the presence of such a sinusoidal signal (whose amplitude and phase have to be retrieved) inside the whole temporal acquired data. The first step consists in checking that the signal frequency remains constant all over the acquisition window. In fact, if the

time window width becomes large (mainly according to the seeding particle density at measurement point), this frequency could suffer a drift. Therefore, the sinusoidal signal feed is also reacquired and these acquisition points are folded into one cycle: if the drift exists, it will induce an uncertainty interval around the pure sine. Then, a frequency correction which minimizes such spread is introduced and a corrected frequency is obtained.

Figure 9-a shows the total, coherent and mean velocities for a single spatial position, while in Figure 9-b the corresponding histogram points out the gaussian nature of the velocity distribution. In Figure 9-a, the velocities have been folded over one period as a function of the phase, in order to enhance readibility. It can be noticed that the coherent velocity component is rather smaller than the turbulent one, suggesting that, in order to reduce the error in the coherent component, a large number of particle velocities is needed. This can also be appreciated from Figure 8, where the amplitude and phase of the coherent velocity have been traced as a function of the number of measured particles through the volume of measurement. The subscript N represents the velocity measured for a given number N of particles while the subscript s indicates the final 'steady' value. We can see a convergence towards the steady value as the number of retrieved particles increases.

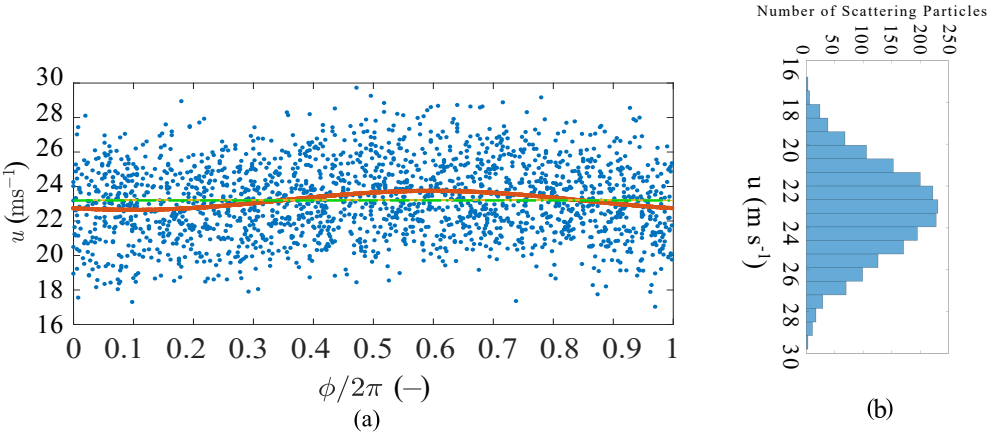

Figure 8: Example of retrieved fluctuating horizontal velocity at a given position in space (a) and relative histogram (b). The total acquired and the reconstructed coherent velocities are shown in dots and solid line, respectively, after being carried over a single (nondimensionalised) time period. Finally, the dash-dotted line represents the time-averaged velocity.

Finally, the reconstruction of the coherent velocity in the form of Eq. 5

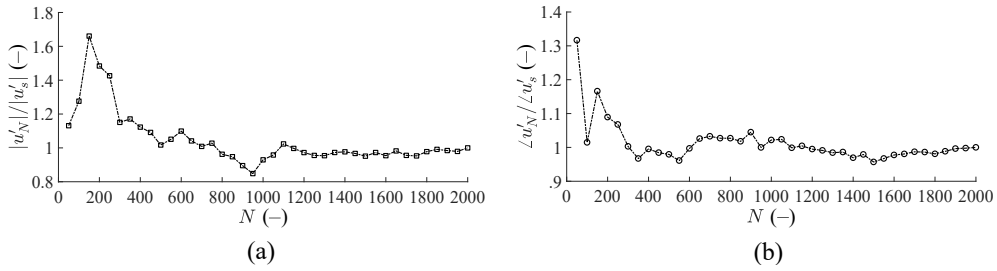

Figure 9: Retrieved amplitude (a) and phase (b) of the vertical fluctuating velocity at a given position in space as a function of the number of measured particles.

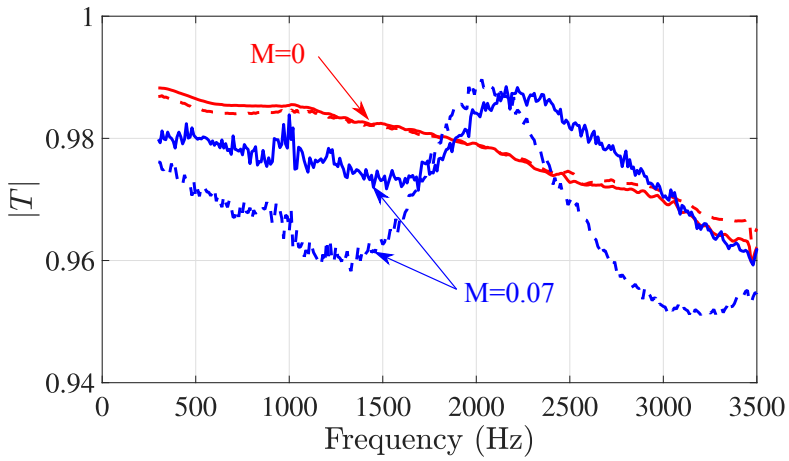

Figure 10: Absolute value of transmission coefficients without flow and with flow (M = 0.07). The continuous lines represent $|T^+|$ and the dashed lines $|T^-|$.

is achieved by the Maximum Likehood (ML) method. As the latter is fully described in [30], the details are not reported here.

4. Results

4.1. Acoustic Measurements

The corrugated plate is first characterised by acoustic measurements. Using the 2 × 4 microphones placed on each side of the plate, the transmission and reflection coefficients are measured with and without flow. The magnitudes of the transmission coefficients (along/against the flow, T^+ and T^- respectively) are given in Figure 10.

In the no-flow case, due to reciprocity, T^+ and T^- are quite identical and the differences between both curves are only due to measurement errors (limited to 0.5%).The deviation to 1 of these curves indicates that visco-thermal losses are present along the walls of the duct corrugated on one of its faces.

When the flow is present, several observations can be made. First, the $|T^+|$ and $|T^-|$ curves are no longer the same, meaning that reciprocity is lost. Secondly, it can be noted that the transmission curves oscillate around the no-flow value. At low frequencies ($f < 1800$ Hz), the attenuation with flow is greater than in the no-flow case. Then, over a specific frequency range (1880 Hz $< f <$ 3100 Hz for T^+ and 1820 Hz $< f <$ 2400 Hz for T^-), the flow reduces the attenuation. This kind of behavior has already been observed in cylindrical corrugated pipes [18] as well as in the effect of flow on a rectangular slot in a wall [31]. The last point to note is that the transmission coefficients always remain below unity. This means that the acoustic losses due to visco-thermal effects are not compensated by hydrodynamic effects. As a result, and contrary to what would happen with a cylindrical corrugated pipe with similar cavities [18], this plate cannot start a whistling process at this flow velocity. This is mainly due to the fact that, unlike a cylindrical pipe where the entire inner surface is corrugated, only the lower quarter of the channel is corrugated here. The Strouhal number at the frequency ($f = 2200$ Hz) for which the hydrodynamic amplification is maximum for T^+ is given by

$$St = \frac{fW}{U_m} = 0.37,$$

where $W = 4$ mm is the cavity width in the flow direction and $U_m = 24$ m s^{-1} is the mean velocity of the flow. Since this value is close to that found in cylindrical pipes ($St \simeq 0.4$, [6, 18]), it can be assumed that the same underlying physical phenomenon occurs in the two-dimensional (2D) case and in the cylindrical case.

From the scattering matrix measurement, it is also possible to estimate the sound power produced (or absorbed) at each frequency by the grazing flow. The ratio of the produced sound power to the incident sound power is given by [32]:

$$\mathcal{P}^{\pm} = |T^{\pm}|^2 + \frac{(1 \mp M)^2}{(1 \pm M)^2}|R^{\pm}|^2 - 1. \tag{6}$$

The difference between the $\mathcal{P}^{\pm}$ evaluated with and without flow gives the

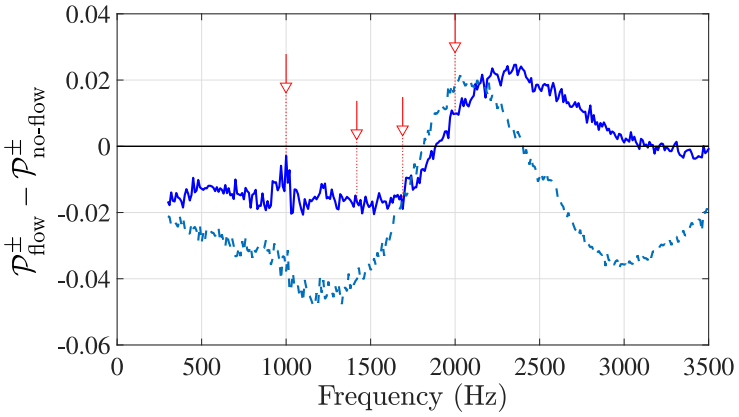

Figure 11: Normalized sound power generated by the grazing flow (M = 0.07). The solid line corresponds to the flow with incident sound in the same direction and the dashed lines to the case where waves travel against the flow. The red dashed arrows point out the frequencies at which the LDV measurements were carried out.

sound power produced by the flow and normalized by the incident sound power. This is shown in Figure 11.

4.2. LDV Results

In this section, the interactions between acoustics and hydrodynamics are investigated using LDV. First, it is possible to see in Figure 12(a) that the periodic velocity field is well resolved with the LDV technique, except, perhaps, in the vicinity of the cavity walls where the measurements are slightly under-resolved. Each pixel in the Figure 12(a) represents a measured value of the vertical periodic velocity $v'/|u'_{\text{ref}}|$. The measured coherent velocities have been nondimensionalised with the respective horizontal coherent velocity at the reference position u_{ref} in order to have a proper comparison between the sets of measurements.

The periodic field is characterized by very clear structures that move horizontally at the cavity lid. Figure 12(b,c) gives the amplitude and the phase of the periodic vertical velocity, respectively, along the cavity which is represented for six horizontal lines corresponding to the axis y = 0, 0.1 ... 0.5 mm (y = 0 mm is the surface of the plate). The slope of the phase indicates the convection velocity of the structures. In this particular case, the variation of the phase is nearly linear, indicating a constant convection velocity given by the slope of the straight line. Surprisingly, the maximum

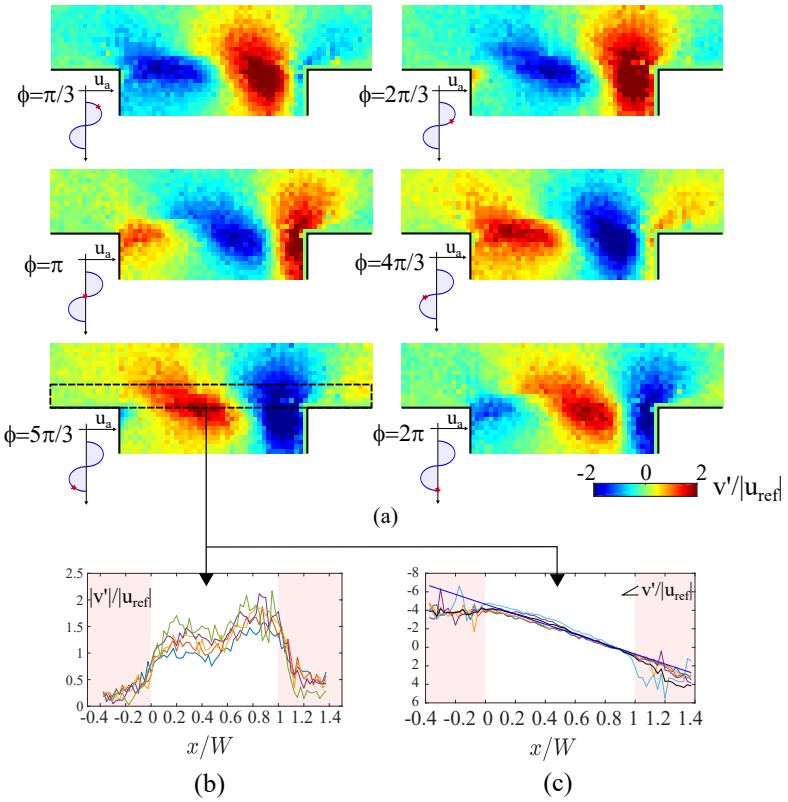

Figure 12: Normalized vertical periodic velocity $v'/|u'_{\mathrm{ref}}|$ colormaps (a) at different relative phases: $\phi_s = \pi/3, 2\pi/3 ... 2\pi$ for the upstream 2000 Hz source position and M =0.07. Vertical periodic velocity modulus (b) and phase (c) along the six horizontal lines corresponding to y = 0, 0.1, ... , 0.5 mm. The thick black line in (c) is the average over the six values and the blue straight line is a linear fit.

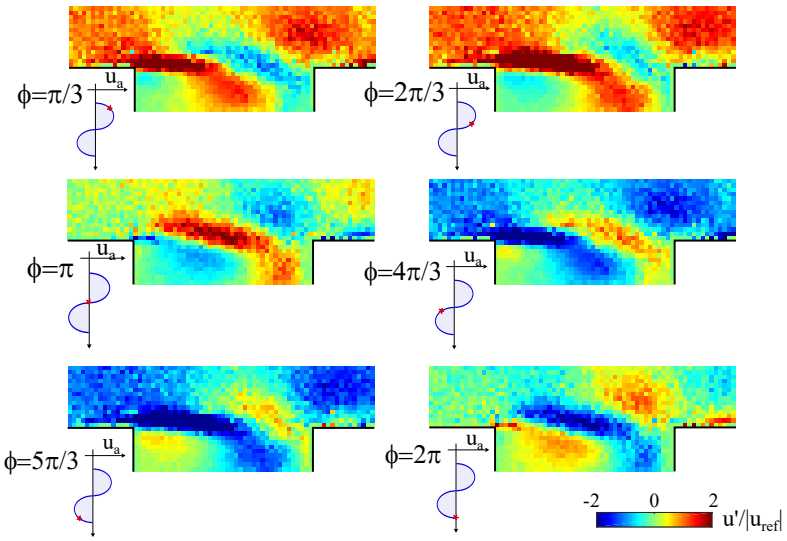

Figure 13: Normalized horizontal periodic velocity $u'/|u'_{\text{ref}}|$ colormaps at different relative phases: $\phi_s = \pi/3, 2\pi/3...2\pi$ for the upstream 2000 Hz source position and M =0.07

amplitude of v' is rather constant over the length of the cavity as can be seen in Figure 12(b). In general, an exponential increase of the disturbance is expected, whereas here there is only a slight increase over the length of the cavity. In Figure 13, the horizontal coherent velocity is shown. Here, the coherent structures are more elongated in the horizontal direction and their amplitude decreases when arriving close the trailing edge of the cavity due to the presence of the wall.

The coherent vorticity $\omega' = \partial_y u' - \partial_x v'$, nondimensionalised by the reference vorticity $\omega_{\text{ref}} = |u_{\text{ref}}|/W$, is depicted in Figure 14. This vorticity is computed using the central difference for inner data points and using one-sided differences for the edges of the domain. The periodic vorticity is tightly packed at the leading edge of the cavity (w.r.t. the trailing edge) and the phase has the same linear variation as the vertical velocity. Then, in this linear regime, the measured structures are associated with a vortical hydrodynamic perturbation at the leading edge of the cavity. However, periodic vorticity cannot be considered to be concentrated on an infinitely thin line nor at a point. Thus, none of the simplest models, i.e. shear layer oscillations that increase exponentially with distance from the upstream edge [33, 34] or shear layer oscillations that break down into discrete vortices [14], can be applied here. This is due to the finite thickness of the mean shear layer with

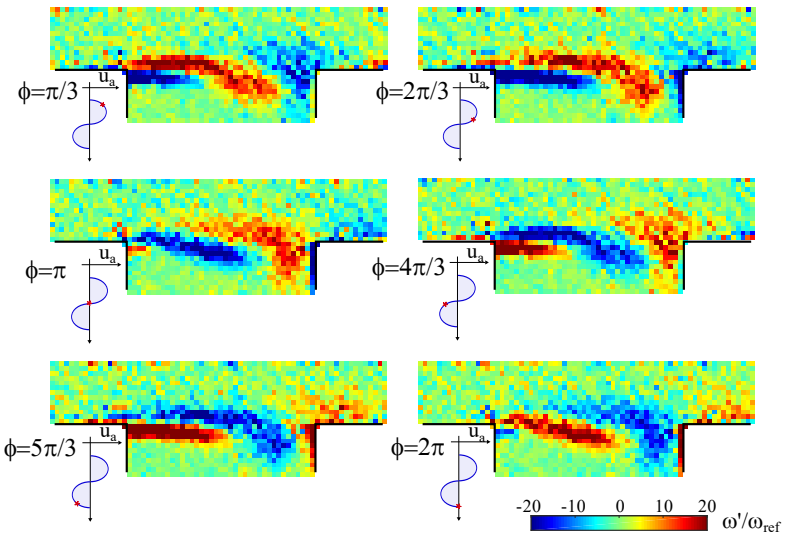

Figure 14: Normalized vorticity $\omega'/\omega'_{\text{ref}}|$ colormaps at different relative phases: ϕ_s = $\pi/3, 2\pi/3...2\pi$ for the upstream 2000 Hz source position and M =0.07.

respect to the size of the cavity [15].

Furthermore, from Figure 15, we can see that the vorticity structure is composed of counter-rotating vorticity zones tightly packed. At the leading edge, the vorticity is governed by the term $-\partial u'/\partial y$, while, at the trailing edge, it is the term $\partial v'/\partial x$ which prevails. This could be expected, as at the leading edge the sudden expansion along y is the dominating effect, while at the trailing edge the hard wall imposes a strong x gradient. At the beginning of the cavity, we can observe counter rotating vorticity zones (almost) stacked on top of each other. This is due to the u' profile shape which is not monotonic: instead, a crest shape can be observed, whose maximum is around y = 0 (as shown in Figure 15-inset). This is due to the interaction between the potential acoustic velocity (which would be infinite at the sharp edge) and the hydrodynamic velocity through the Kutta condition. Therefore, when u' is positive, this translates in a positive vorticity area on top of a negative one. Near the trailing edge, instead, the vorticity distribution ω' is similar to the v' distribution (as here the term $\partial v'/\partial x$ dominates), where wider opposite sign zones follow each other.

To test the linearity hypothesis, the corrugated plate was exposed to two different sound levels, while keeping all other parameters constant. By

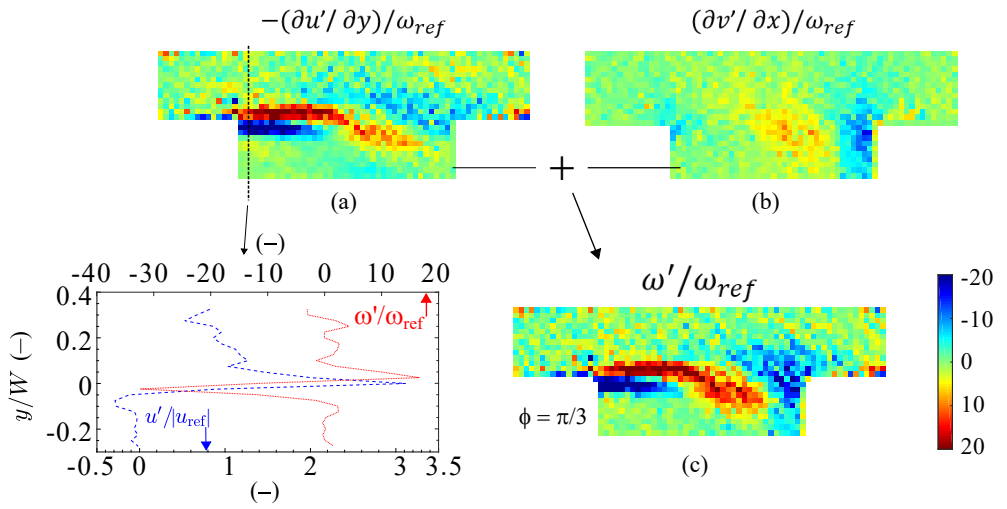

Figure 15: Normalized vorticities (a) $-(\partial u'/\partial y)/\omega_{\text{ref}}$, (b) $(\partial v'/\partial x)/\omega_{\text{ref}}$ and (c) their sum $\omega'/\omega'_{\text{ref}}$ colormaps at ϕ = 0 for the upstream 2000 Hz source position and M =0.07 case. The inset indicates the horizontal $u'/|u_{\text{ref}}|$ velocities and vorticity $\omega'/\omega_{\text{ref}}$ along x = 0.

decreasing the voltage supplied to the source, the horizontal sound velocity in the reference box u'_{ref} was reduced from 0.56 m s^{-1} to 0.24 m s^{-1} (7.5 dB decrease, see table 1). Testing the linearity hypothesis is particularly important because, in order to work with the largest possible value of the signal-to-noise ratio, the ratio u'/U0 must be close to the threshold for which non-linear effects appear, which is of the order of 1% (see Fig. 9 in [18]). In our study, for the highest sound level (140 dB), this ratio is 2% and decreases to 1% for a sound level of 132 dB. The level used is therefore at the upper limit of the level that can be considered to be linear. The colormaps of the vertical periodic velocity normalized by u'_{ref} are presented in Figure 16. Despite some minor differences, the normalized velocities are globally similar, which indicates the linearity of the studied phenomena. It should be noted that in the case of lower amplitudes, the signal-to-noise ratio is lower, which leads to less accurate and more difficult measurements.

In the following subsections, different setup configurations have been studied as shown in the table 1. These configurations have been chosen in order to investigate the effects of the position of the sound source (w.r.t. the direction of the mean flow) and its frequency. Also, a separate subsection is devoted to the discussion of the convective velocity of aeroacoustic structures.

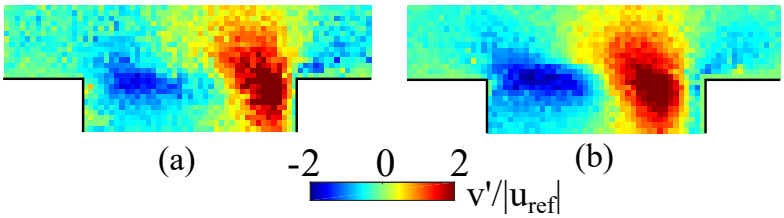

Figure 16: Nondimensionalized vertical periodic velocity colormaps for the (a) low and (b) high amplitude acoustic source cases at $\phi_s = \pi/3$.

Frequency	**Source Position**	**Sound Level**	**Acoustic Amplitudes**
f = 1000 Hz	Upstream	140 dB	0.56 m s^{-1}
f= 1400 Hz	Upstream	140 dB	0.56 m s^{-1}
	Downstream	140 dB	0.56 m s^{-1}
f = 1700 Hz	Upstream	140 dB	0.56 m s^{-1}
f = 2000 Hz	Upstream	140 dB	0.56 m s^{-1}
	Upstream (low amp)	132.5 dB	0.24 m s^{-1}
	Downstream	140 dB	0.56 m s^{-1}

Table 1: LDV measurement configurations

4.2.1. Frequency Effects

In this section, we analyze the corrugated plate for two different values of the source frequency: 1400 and 2000 Hz. These two configurations are detailed in Table 1 and the only difference is the source frequency: the value of 2000 Hz corresponds to a (nearly) maximum produced acoustic power (w.r.t the baseline no-flow case), while the 1400 Hz corresponds to an absorbed one. From Figure 17, it is possible to appreciate how frequency difference creates a different relative position of the maxima and minima in the velocity field, for the $f = 2000$ and 1400 Hz upstream source cases. Furthermore, we can see that in the 2000 Hz case, a third positive velocity area appears at the trailing edge of the cavity. It is important to outline that the velocity distribution is directly responsible for acoustic production, as shown in the later Section 5. These structures are characterised by a wavelength λ_i which is given by

$$\lambda_i = \frac{U_c}{f_s} \tag{7}$$

where f_s is the source frequency and U_c is the velocity at which such structures are convected downstream, i.e. the convective velocity. For the 1400 Hz case (17-a), this length is $\lambda_1/2 \approx 2.7$ mm while for the 2000 Hz case (17-b) the length is $\lambda_2/2 \approx 2.2$ mm. On the other hand, the ratio between the lengths λ_1 and λ_2 is not exactly equal to the inverse of the frequency ratio, as one might expect: while the ratio of lengths is ≈ 1.23, the inverse ratio of frequency is ≈ 1.43 suggesting that the velocity of propagation of disturbances is a function of frequency. This is shown in Figure 18, where the vertical coherent velocity phases have been traced along the cavity. As this slope is directly linked to the convective velocity through the acoustic frequency as

$$U_c = \frac{2\pi f_s W}{|\Delta\phi/W|} \tag{8}$$

where now $|\Delta\phi/W|$ is the phase slope, we can see that the convective velocity grows with the signal frequency at most 16%. This result challenges the common assumption, when modeling the shear layer amplification in the linear regime, that this velocity is constant.

4.2.2. Acoustic Source Position Effect

In this paragraph, we are interested in analysing the effect of the of the relative direction of propagation between the acoustic wave and the flow. The main discrepancy introduced by the different propagation direction of

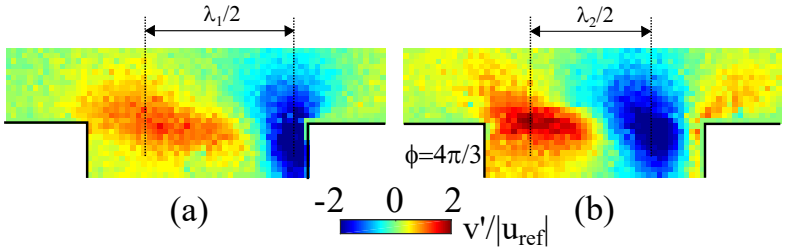

Figure 17: Vertical periodic velocity (Real part) colormaps for the f_s = 1400 (a), 2000 (b) Hz upstream cases, $\phi = 4/3\pi$

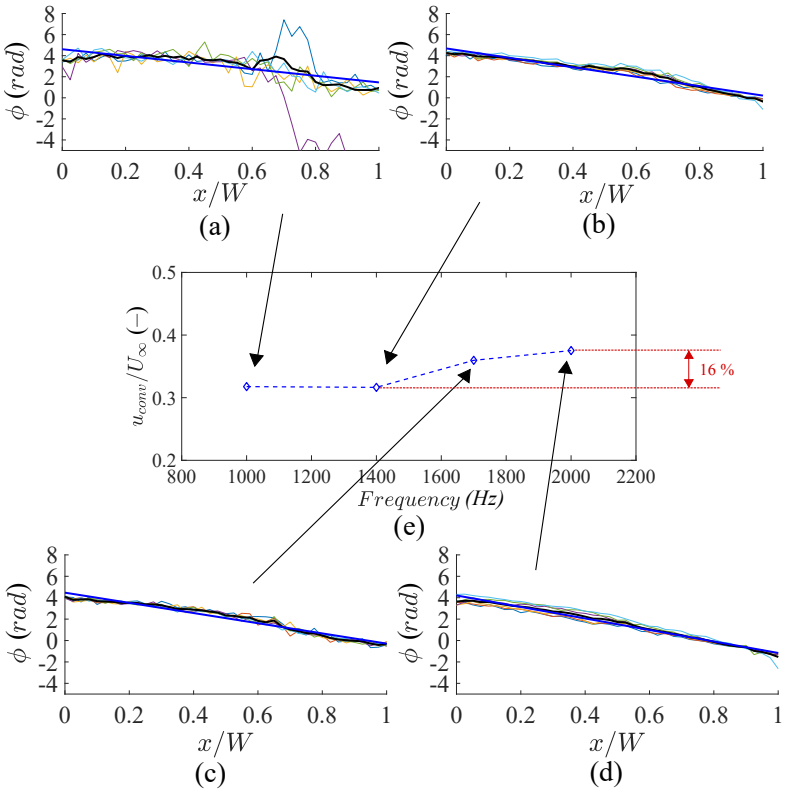

Figure 18: Vertical periodic velocity phases (a-d) along the six horizontal lines corresponding to y = 0, 0.1, ... , 0.5 mm for the f_s = 1000, 1400, 1700, 2000 Hz upstream cases. In (e) the convective velocities calculated from the phase slopes for the same four cases are shown.

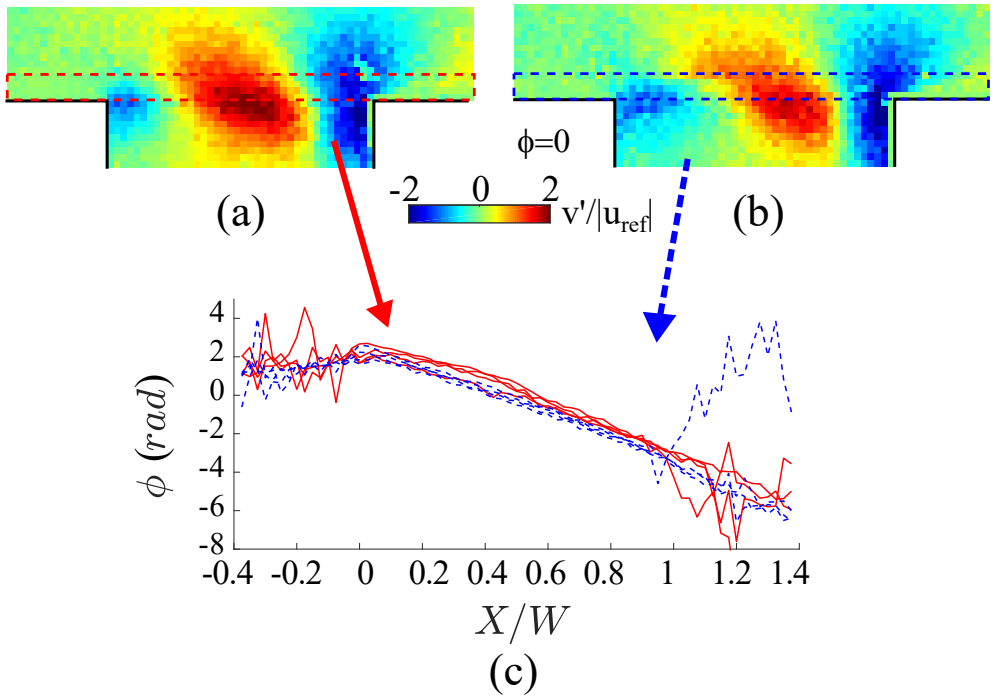

Figure 19: Vertical periodic velocity (Real part) colormaps for the (a) downstream and (b) upstream $f_s = 2000\ Hz$ cases, $\phi = 0$. In (c) the vertical periodic velocity phases calculated along the corresponding indicated lines are also shown

the acoustic wave is a phase difference. As the measurements are taken w.r.t. the reference box, we can see that, at the same phase reference, for the downstream case, the velocity structures are lagging behind by a small phase difference. This can be directly seen from the periodic velocity colormaps, as done in the precedent paragraph and shown here in Figure 19, which show the vertical periodic velocity for the two cases. It can be seen that the same field structures are retrieved and in the downstream case the cores of these structures are slightly closer to each other (again, from Eq. 7, we can measure $\lambda_d = 2$ mm for the downstream case while $\lambda_u = 2.2$ mm for the upstream one). The same results, not shown here, have been obtained at the forcing frequency of $f_{ref} = 1400$ Hz.

5. Acoustic Power

Considering an homoentropic flow (with the additional constraint of a low Mach number), Howe [35] computed the acoustic power formulation as follows:

$$\langle P_H \rangle = -\int_V \rho_0 \langle (\boldsymbol{\omega} \times \mathbf{u}) \cdot \mathbf{u}_a \rangle \mathrm{d}V = \int_V \langle (F_x u_a + F_y v_a) \rangle \mathrm{d}V, \tag{9}$$

where $\boldsymbol{\omega} = (\Omega_0 + \omega')\,\mathbf{z}$, $\mathbf{u} = (U_0 + u')\,\mathbf{x} + (V_0 + v')\,\mathbf{y}$ and $\mathbf{u}_a = u_a\mathbf{x} + v_a\mathbf{y}$ are respectively the total vorticity, the total velocity and the acoustic (i.e. potential) velocity of the flow, while $\mathbf{F} = F_x\mathbf{x} + F_y\mathbf{y} = -\rho_0\,(\boldsymbol{\omega} \times \mathbf{u})$ is the Coriolis force vector. The symbol $\langle\ \rangle$ represents the average over one time period. In the case of complex functions, such average can be directly computed as (e.g. for the first term inside the integral of Eq. 9) :

$$\langle F_i u_a \rangle = \frac{1}{2}\,\mathrm{Re}\left(\bar{F}_i u_a\right) \tag{10}$$

for $i = x, y$ and $\bar{F}_i$ is the complex conjugate of vector F_i.
It is interesting to notice that the vector product $\mathbf{F} = (F_x, F_y) = -\rho_0\,(\boldsymbol{\omega} \times \mathbf{u})$ is composed of an horizontal and a vertical Coriolis force term (by unit volume). As explained in section 2.4, since the acoustic velocity in Eq. 9 cannot be measured directly, a COMSOL frequency domain simulation was carried out to solve the Helmholtz equation. Furthermore, the acoustic power is nondimensionalised w.r.t. a reference power calculated as follows:

$$P_a = \frac{|u_{\mathrm{ref}}|^2 \rho_0 c_0}{2} \tag{11}$$

since, in a centerline position, the relationship $p_{\mathrm{inf}}/u_{\mathrm{ref}} = \rho_0 c_0$ is a fair assumption and the periodic horizontal velocity equals the acoustic velocity, i.e. $u_{\mathrm{ref}} \approx u_a$.
It should also be noted that from the vector $\mathbf{F} = -\rho_0\,((\boldsymbol{\Omega}_0 + \boldsymbol{\omega}') \times (\mathbf{U}_0 + \mathbf{u}'))$, when the time average inside Eq. 9 is carried out, the inner product of the mean values do not contribute, while, at order one, the inner product of the coherent terms can be neglected. Then, each component of the vector $\mathbf{F}$ can be written as

$$F_x = \rho_0\,(\omega' V_0 + \Omega_0 v') \tag{12}$$

$$F_y = -\rho_0\,(\omega' U_0 + \Omega_0 u') \tag{13}$$

Therefore, each component of the Coriolis force can be split into two contributions and the total acoustic power will result from their inner product with the acoustic velocity. In other words, the more the Coriolis vector is aligned along the acoustic velocity streamlines, the larger the acoustic production will be. We can then define, in a definitely improper but practical way, an 'horizontal' and 'vertical' acoustic power as the contributions due to the corresponding horizontal and vertical Coriolis forces. In Figure 20, these components are shown, time-averaged, for the 2000 Hz upstream source case, together with the total acoustic power distribution. It is interesting to notice that the two contributions inside each component of the Coriolis force are of the same order of magnitude, while, on the other hand, they are not at all similarly distributed. In the following sections we consider the spatial distributions of the four contributions for the f = 2000 Hz upstream source case. This frequency corresponds to a net positive normalized sound-power generation.

5.1. Acoustic Power $\rho_0(\omega' V_0)u_a$ contribution

The acoustic power generated by the Coriolis component $\rho_0(\omega' V_0)$ is $\rho_0(\omega' V_0)u_a$ and is shown, averaged over one period, in Figure 20-b. As we can see, this power contribution is very small at all points in the flowfield. By looking at the mean vertical velocity V_0 (see Figure 5), we can see that this velocity is small (when compared with U_0) and confined inside the cavity, while almost zero elsewhere. At the same time, the coherent vorticity ω' is concentrated inside the shear layer, which is thin along the cavity lid (see Figure 14). Only near the trailing edge, the vorticity slightly spreads inside the cavity as the shear layer becomes thicker. Then, these terms cannot interact with each other: the Coriolis component $\rho_0(\omega' V_0)$ and, as a consequence, the corresponding acoustic power $\rho_0(\omega' V_0)u_a$, will be very small. These observations would probably still hold when the frequency changes.

5.2. Acoustic Power $\rho_0(\Omega_0 v')u_a$ contribution

The term $\rho_0(\Omega_0 v')u_a$ is the one which gives the global structure to the total horizontal power, as can be observed from Figure 20-a,c (time averaged) and Figure 21 for $\phi = \pi/3$. In this case, we can identify two dinstinct absorption and production areas which are isolated from each other. The mean vorticity Ω_0 is shed clockwise (i.e. negative) at the leading edge discontinuity. Furthermore, from Figure 12, we can see that the velocity v' has

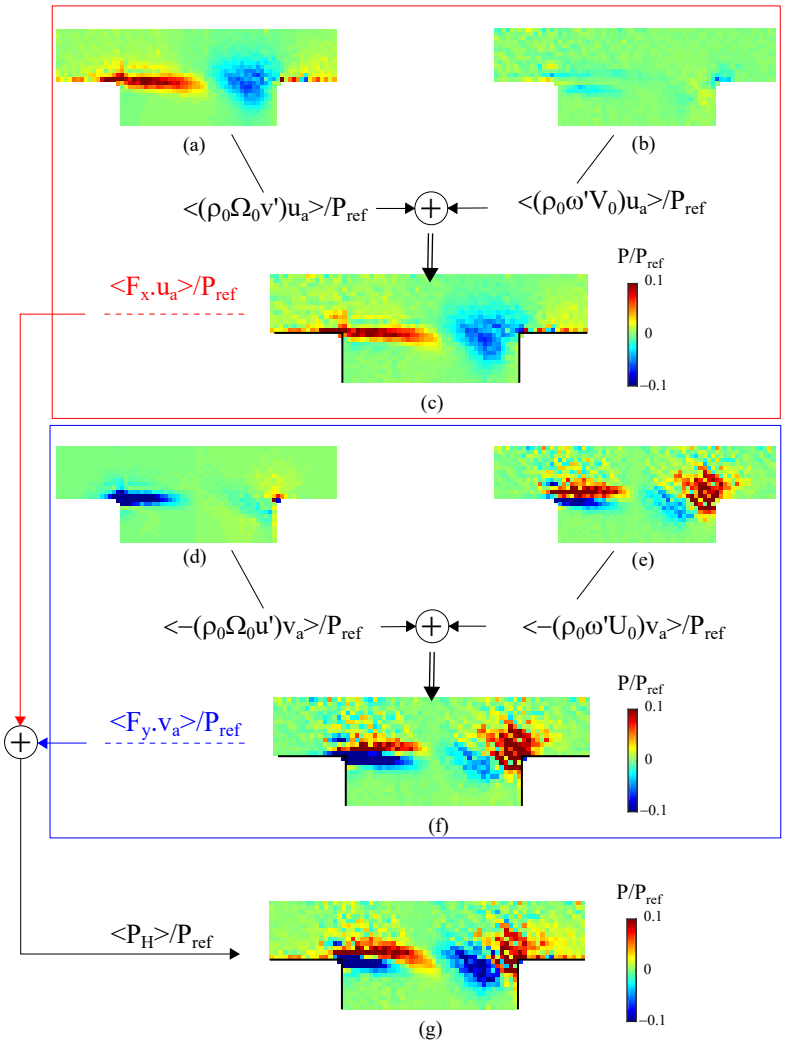

Figure 20: Normalised acoustic power due to the horizontal (c) and vertical (f) Coriolis force, respectively split into their two main contributions (a-b) and (d-e) following Eq. 13, for the 2000 Hz case. Finally, the total acoustic power (g) is shown.

430 a very small phase gap with the vertical acoustic velocity v_a and therefore the two components have the same sign. Therefore, when the vertical acoustic velocity v_a is negative at the leading edge, the Coriolis term $\rho_0(\Omega_0 v')$ is here positive. At the same time, the horizontal acoustic velocity u_a here is positive and so is the contribution $\rho_0(\Omega_0 v')u_a$. Meanwhile, at the trailing

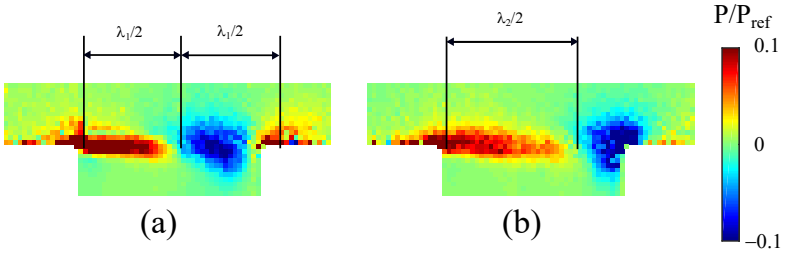

Figure 21: The acoustic power contribution $(\Omega_0 v')u_a$ for the (a) 2000 Hz and (b) 1400 Hz upstream case at $\phi = \pi/3$.

.

edge, the vertical velocity v' is now positive (see Figure 12) while Ω_0 is still negative and the Coriolis term $\rho_0(\Omega_0 v')$ is therefore negative. As the horizontal acoustic velocity u_a is here still positive, an acoustic absorption will be observed. From Figure 21, we notice that the main change with frequency is the absorption position at the trailing edge. This is due to the fact that the length λ_i is influenced by the frequency while the phase gap between the acoustic and coherent velocities is not. Furthermore, the fact that the magnitudes of the velocities v' (see Figure 13-b) and u_a don't change along the cavity and that the Ω_0 integral along the y-axis is supposed to stay constant while moving from the leading onto the trailing edge, suggests why the contribution $\rho_0(\Omega_0 v')u_a$ does not show a dependency on frequency (see Figure 24).

In Figure 21, the comparison of the $\rho_0(\Omega_0 v')u_a$ contribution for the 2000 and 1400 Hz case is shown, at $\phi = \pi/3$.

5.3. Acoustic Power $-\rho_0(\Omega_0 u')v_a$ contribution

In order to describe the $-\rho_0(\Omega_0 u')v_a$ contribution, the same considerations that were made above for the Ω_0 term apply also here. At the leading edge, it can be seen from Figure 13 that the horizontal coherent velocity u' is positive when the acoustic velocity v_a is negative. Then, in this position, the Coriolis force is positive when it interacts with a negative (downward) acoustic velocity, and viceversa. Thus, a negative acoustic contribution $-\rho_0(\Omega_0 u')v_a$ is induced. Also, we can see from Figure 13, that the velocity u' is always very small close to the trailing edge of the cavity, due to the presence of the cavity hard wall. This explains why, in Figures 22, the acoustic power at the trailing edge is very small. From this follows also why this contribution is negative over the period and for all frequencies (see Figure 24).

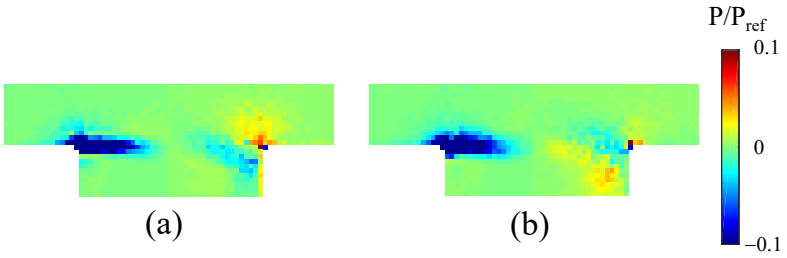

Figure 22: The acoustic power contribution $(-\Omega_0 u')v_a$ for the (a) 2000 Hz and (b) 1400 Hz upstream case at $\phi = \pi/3$.

.

In Figure 22, the comparison of the $-\rho_0(\Omega_0 u')v_a$ contribution for the 2000 and 1400 Hz case is shown, for $\phi = \pi/3$.

5.4. Acoustic Power $-\rho_0(\omega' U_0)v_a$ contribution

If we look at the acoustic power contributions from the vertical Coriolis force F_y (see Figure 20-e,f), the term $-\rho_0(\omega' U_0)v_a$, which is the largest contribution, appears to be the one that gives the power distribution its complexity. Inside the Coriolis force $-\rho_0(\omega' U_0)$, the mean horizontal velocity U_0 is positive at all points. Moreover, its magnitude does not change strongly along the cavity length and these variations are confined in a very thin shear layer at the cavity lid. The largest thickness of this layer is around 1 mm (see Figures 5a-c). Therefore, the Coriolis contributions inside the cavity are filtered out and their sign are opposite to the vorticity one. Then, at the leading edge, two counter rotating vorticity zones (as explained before, see Figure 15) will interact with the v_a component, giving opposite acoustic powers, of which the positive one (over the cycle) is larger. At the trailing edge, the ω' structure will vary with frequency as the v' structure does. In order to have production at the trailing edge, vorticity here should have the same sign of the prevailing vorticity at the leading edge, as here the velocity v_a has an opposite sign. This should happen optimally when the vorticity period is $\approx 2(W/U_c)/3$. For the 2000 Hz case, the period is slightly larger at $\approx W/U_c$. Thus, we are not at the point of maximal production, but two co-rotating vorticity areas at the edges of the cavity are however allowed. When the period becomes larger (e.g. for the 1400 Hz case), this is not possible anymore and the vorticity at the leading and trailing edges will have opposite sign, which translates in absorption at the trailing edge. In Figure

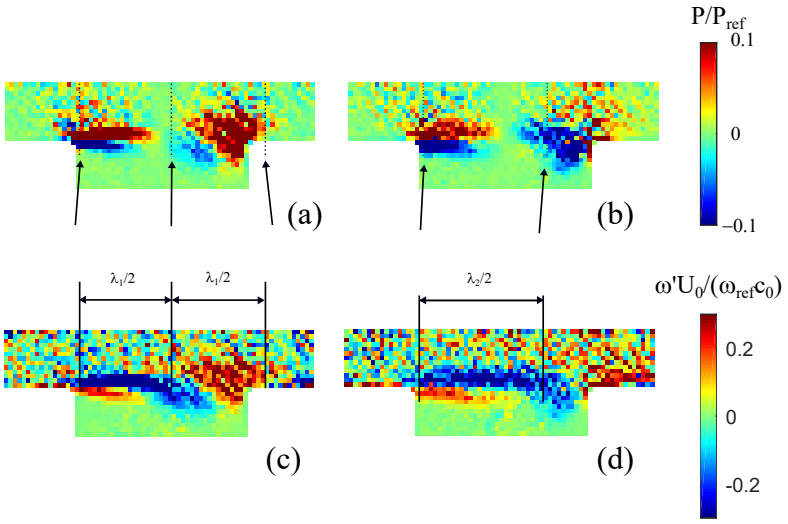

Figure 23: The acoustic power contribution $(-\omega' U_0) v_a$ for the (a) 2000 Hz and (b) 1400 Hz upstream cases at $\phi = \pi/3$. In (c) and (d) the Coriolis force $-\rho_0(\omega' U_0)$ is shown for the 2000 and 1400 Hz cases, respectively, at the same phase.

.

23, the comparison of the $-\rho_0(\omega' U_0) v_a$ contribution for the 2000 and 1400 Hz case is shown, for $\phi = \pi/3$.

5.5. Acoustic Power Contributions: Summary

In summary, it has been shown that the acoustic power related to the horizontal Coriolis force is on the average close to zero: this is because the component $\rho_0(\omega' V_0) u_a$ is negligible everywhere in the aeroacoustic field while the integral of the $\rho_0(\Omega_0 v') u_a$ contribution over the period is zero, even if local production and absorption areas are present at the cavity edges. Therefore, it is the vertical Coriolis force contribution who finally determine the behaviour of the corrugated wall. In this contribution, the $-\rho_0(\Omega_0 u') v_a$ term is responsible for an absorption area at the leading edge which is always negative with frequency. Then, the frequency dependency of the absorption and production mechanisms derives from the $-\rho_0(\omega' U_0) v_a$ term, which is also responsible for the complexity of the acoustic power distribution. In this case, the acoustic frequency influences the hydrodynamic wavelength and the coupling with the cavity length: when the wavelength is close to the $2W/3 + nW$ value (with n integer), global acoustic production is possible.

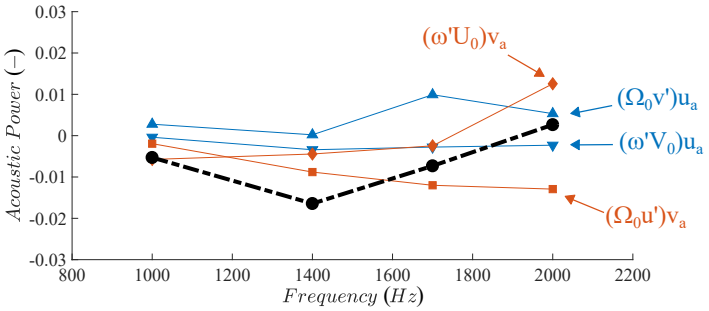

Figure 24: Acoustic Powers contributions $(\Omega_0 v')u_a$ and $(\omega' V_0)u_a$ (filled upward and downward triangles, respectively) and contributions $(\Omega_0 u')v_a$ and $(\omega' U_0)v_a$ (filled squares and diamonds, respectively) for the f = 1000, 1400, 1700, 2000 upstream source cases. Also, the total acoustic power is shown in filled circles

The complexity resulting from the different contributions to acoustic production cannot be captured through the models usually employed when whistling is present. The simplifications adopted in this case are not applicable here: vorticity cannot be considered concentrated in a single moving vortex (like in the SCV model) as it is distributed over the entire cavity. Furthermore, it has a complex distribution perpendicular to the shear layer while spreading out along the cavity, a behaviour which is not taken into account in the SDV model. This shows that the models usually adopted in presence of the whistling cease to be applicable in the linear regime. This is also confirmed by the optical results of [10, 11]. In [10], it is shown that the vorticity field is driven by a large amplitude vortex that extends over the cavity. In [11], the time-averaged acoustic power field is calculated in a similar way to the present work. It is possible to appreciate how, even when the second hydrodynamic mode dominates and the acoustic field can be considered as linear, the source-sink pairs can be identified and still remain separated from each other. This is a consequence of the large-scale vortices present in the flow field, as confirmed by the authors.

5.6. Effect of Sound Propagation Direction

As explained before (see section 4.2.2), the main effect of changing the acoustic source position is the introduction of a phase difference in the hydrodynamic structures. This influences the acoustic production, as shown in Figure 25, where the total acoustic production for an acoustic source frequency of 2000 Hz is presented, for both a relative upstream and downstream

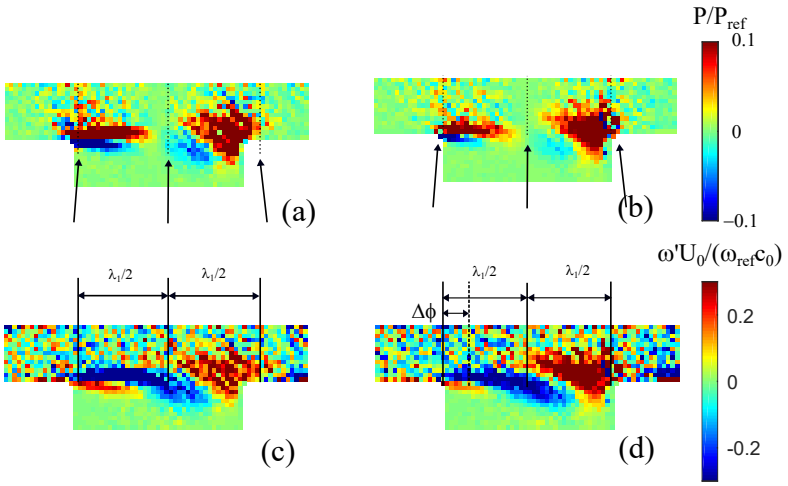

Figure 25: The acoustic power contribution $(-\omega' U_0) v_a$ for the 2000 Hz (a) upstream and (b) downstream case at $\phi = \pi/3$. In (c) and (d) the Coriolis force $-\rho_0(\omega' U_0)$ is shown for the 2000 Hz upstream and downstream cases, respectively, at the same phase.

source positions. Indeed, the phase difference for the downstream case shifts upstream the production region at the trailing edge, which increases the overall interaction. At the same time, the differences at the leading edge appears negligible. This is highlighted in Figure 25-c,d, where the nondimensionalised vertical Coriolis force $-\rho_0(\omega' U_0)$ is shown. There, it appears that the main difference in the Coriolis distribution is the upstream shift of the trailing peak, which will therefore have a larger contribution.

6. Conclusions

The aeroacoustic field around a corrugated wall in a grazing flow configuration has been studied. First, we investigated the behaviour of the corrugated plate over a wide frequency band by measuring the scattering matrix of the test sample. This allows to understand how the corrugations behaved globally and whether or not the Strouhal numbers corresponding to the characteristic frequencies were similar to the ones obtained in previous studies. Indeed, as expected from the literature, characteristical frequency ranges where transmission coefficients were higher/lower (namely "gain/loss" zones) than the corresponding no-flow configuration have been identified. For all cases, however, the transmission coefficients stay below unity as opposed to other studies. This is mainly because in the present setup the corrugated

plate is covering only one side of the waveguide. Then, the acoustic source frequency and the flow Mach number have been set in order to investigate four points between the "gain" and the "loss" zones using the optical LDV technique. The main quantities which identify the fluid-dynamic as well as the acoustic fields have been fully resolved. In particular, coherent velocity structures are clearly visible and their propagation velocity appears to be weakly function of frequency. Also, the coherent vorticity, which is directly responsible for the acoustic power production/absorption is well resolved. However, it is not possible to isolate distinct zones of absolute acoustic power absorption or production as these are usually entangled in a complex form due to the acoustic forcing of the hydrodynamic velocity at the leading edge. However, even in this complex scenario, it is possible to appreciate how a change in frequency (i.e. a different separation between the velocity structure) or in the source position (i.e. a relative space shift in the velocity structures) can explain the gain/loss mechanism. These results also indicate that either one of the 1D models (DV/CV models) is hardly going to give good predictions. First, source/sink contributions are not distinct between each other in the measurement volume. Furthermore, the entanglement at the leading edge cannot be considered in a 1D modeling, as well as the power contribution from the longitudinal Coriolis term. Also, the contribution to the vertical Coriolis term of the horizontal coherent velocity (i.e. $(\Omega_0 u')$) is somewhat non negligible and usually not considered. All these contributions are necessarily not taken into account in a 1D model, which suggests that such a model would not be a good predictor of the acoustic power. Further studies will therefore need to account for these discrepancies in order to improve the modeling accuracy. Hopefully, open access to the dataset [21] will be beneficial to the combined efforts towards this scope.

7. Acknowledgments

This research was supported by the European Union's Horizon 2020 research and innovation programme under the Marie Skłodowska-Curie grant agreement No 722401("SmartAnswer") (https://www.h2020-smartanswer.eu/)

References

[1] F. S. Crawford, Singing corrugated pipes, Am. J. Phys. 42 (4) (1974) 278–288. doi:10.1119/1.1987673.

[2] D. Rockwell, E. Naudascher, Review - Self-Sustaining Oscillations of Flow Past Cavities, J. Fluids Eng. 100 (June) (1978) 14. doi:10.1115/1.3448624.

[3] Y. Nakamura, N. Fukamachi, Sound generation in corrugated tubes, Fluid Dyn. Res. 7 (5) (1991) 255 – 261. doi:10.1016/0169-5983(91)90018-E.

[4] V. F. Kopiev, M. A. Mironov, M. A. Yakovets, Flow noise in a corrugated pipe in terms of the theory of instability waves, Acoust. Phys. 61 (5) (2015) 499–503. doi:10.1134/S1063771015050115.

[5] A. Lapin, V. F. Kopiev, Admittance of a groove on a rigid surface under a grazing flow, Acoust. Phys. 49 (1) (2003) 75–80. doi:10.1134/1.1537391.

[6] G. Nakiboğlu, S. Belfroid, J. Golliard, A. Hirschberg, On the whistling of corrugated pipes: effect of pipe length and flow profile, J. Fluid Mech. 672 (2011) 78–108.

[7] E. Salt, S. Mohamed, D. Arthurs, S. Ziada, Aeroacoustic sources generated by flow–sound interaction in a t-junction, J. Fluids Struct. 51 (2014) 116 – 131. doi:10.1016/j.jfluidstructs.2014.08.005.

[8] D. Tonon, B. Landry, S. Belfroid, J. Willems, G. Hofmans, A. Hirschberg, Whistling of a pipe system with multiple side branches: Comparison with corrugated pipes, J. Sound Vib. 329 (8) (2010) 1007–1024. doi:https://doi.org/10.1016/j.jsv.2009.10.020.

[9] A. A. Shaaban, S. Ziada, Fully developed building unit cavity source for long multiple shallow cavity configurations, Phys. Fluids 30 (8) (2018). doi:10.1063/1.5041751.

[10] M. El Hassan, L. Labraga, L. Keirsbulck, Aero-acoustic oscillations inside large deep cavities, Proc. 16th Australas. Fluid Mech. Conf. AFMC (Gold Coast, Australia) (December 2007) 421–428.

[11] F. R. Verdugo, R. Camussi, G. J. Bennett, Aeroacoustic source characterization technique applied to a cylindrical Helmholtz resonator, 18th Int. Congr. Sound Vib. ICSV 2011 1 (Rio de Janeiro, Brazil) (July 2011) 349–356.

[12] M. Howe, Contributions to the theory of aerodynamic sound, with application to excess jet noise and the theory of the flute, J. Fluid Mech. 71 (04) (1975) 625–673.

[13] J. C. Bruggeman, A. Hirschberg, M. E. H. van Dongen, A. P. J. Wijnands, J. Gorter, Self-sustained aero-acoustic pulsations in gas transport systems: Experimental study of the influence of closed side branches, J. Sound Vib. 150 (3) (1991) 371–393. doi:10.1016/0022-460X(91)90893-O.

[14] P. Nelson, N. Halliwell, P. Doak, Fluid dynamics of a flow excited resonance, part ii: Flow acoustic interaction, J. Sound Vib. 91 (3) (1983) 375–402.

[15] J. Bruggeman, A. Hirschberg, M. van Dongen, A. Wijnands, J. Gorter, Flow induced pulsations in gas transport systems: analysis of the influence of closed side branches, J. Fluids Eng. 111 (4) (1989) 484–491.

[16] J. W. Elliott, Corrugated pipe flow, in: Lecture Notes on the Mathematics of Acoustics, pp. 207–222.

[17] J. Bruggeman, Flow induced pulsations in pipe systems, Ph.D. Thesis Technische Hogeschool, Eindhoven (Netherlands). (1987). doi:10.6100/IR264848.

[18] J. Golliard, Y. Aurégan, T. Humbert, Experimental study of plane wave propagation in a corrugated pipe: Linear regime of acoustic-flow interaction, J. Sound Vib. 472 (2020) 115158. doi:https://doi.org/10.1016/j.jsv.2019.115158.

[19] A. Michalke, On spatially growing disturbances in an inviscid shear layer, J. Fluid Mech. 23 (3) (1965) 521–544. doi:10.1017/S0022112065001520.

[20] M. S. Howe, Interaction of sound with solid structures, 2010. doi:10.1017/cbo9780511662898.006.

[21] D. Massimo, Dataset for H2020 Smartanswer Corrugations Experiment (Mar. 2021). doi:10.5281/zenodo.5702563.
URL `https://doi.org/10.5281/zenodo.5702563`

[22] Y. Aurégan, M. Leroux, Experimental evidence of an instability over an impedance wall in a duct with flow, J. Sound Vib. 317 (3-5) (2008) 432–439. doi:10.1016/j.jsv.2008.04.020.

[23] M. Åbom, Measurement of the scattering-matrix of acoustical two-ports, Mechanical systems and signal processing 5 (2) (1991) 89–104.

[24] H. Lin, D. Hsu, J. Su, Particle Size Distribution of Aromatic Incense Burning Products, Int. J. Environ. Sci. 6 (11) (2015) 857–860. doi:10.7763/IJESD.2015.V6.712.

[25] M. Hamdi, M. Havet, O. Rouaud, D. Tarlet, Comparison of different tracers for PIV measurements in EHD airflow, Exp. Fluids 55 (4) (2014). doi:10.1007/s00348-014-1702-z.

[26] A. Melling, Tracer Particles and Seeding for Particle Image Velocimetry, Meas. Sci. Technol pp. 1406-1416, 1997.

[27] A. Hjelmfel, L. Mockros, Motion of Discrete Particles in a Turbulent Fluid, Appl. Sci. Res. 16 (1) (1966) 149–161.

[28] T. V. Karman, Mechanical similitude and turbulence, 1931.

[29] H. Schlichting, K. Gersten, Boundary-Layer Theory, 2017. doi:10.1007/978-3-662-52919-5.

[30] M. E. D'Elia, T. Humbert, Y. Auregan, J. Golliard, Optical measurements of the linear sound-flow interaction above a corrugated plate, in: 25th AIAA/CEAS Aeroacoustics Conference, no. Delft, The Netherlands, 2019, p. 2716.

[31] G. Kooijman, A. Hirschberg, J. Golliard, Acoustical response of orifices under grazing flow: Effect of boundary layer profile and edge geometry, J. Sound Vib. 315 (4-5) (2008) 849–874.

[32] C. Morfey, Acoustic energy in non-uniform flows, J. Sound Vib. 14 (2) (1971) 159–170.

[33] S. A. Elder, The mechanism of sound production in organ pipes and cavity resonators, JASJa 13 (1) (1992) 11–23.

[34] M. S. Howe, Acoustics of fluid-structure interactions, Cambridge university press, 1998.

[35] M. S. Howe, Mechanism of sound generation by low Mach number flow over a wall cavity, J. Sound Vib. 273 (1-2) (2004) 103–123. doi:10.1016/S0022-460X(03)00644-8.